npj Microgravity

https://doi.org/10.1038/s41526-026-00570-8

Article in Press

Comparison of clinostat control strategies to achieve simulated microgravity with uniform gravity vector distribution

Received: 30 August 2025

Accepted: 2 February 2026

Cite this article as: Kim, Y.J., Park, S., Kim, S. Comparison of clinostat control strategies to achieve simulated microgravity with uniform gravity vector distribution. *npj Microgravity* (2026). https://doi.org/10.1038/s41526-026-00570-8

Yoon Jae Kim, Sungwoo Park & Sungwan Kim

Comparison of Clinostat Control Strategies to Achieve Simulated Microgravity with Uniform Gravity Vector Distribution

Yoon Jae Kim[1], Sungwoo Park[2,3] and Sungwan Kim[1,4,*]

[1] Institute of Medical and Biological Engineering, Medical Research Center, Seoul National University, Seoul 03080, Korea

[2] Interdisciplinary Program in Bioengineering, The Graduate School, Seoul National University, Seoul 08826, Korea

[3] Institute of Convergence Medicine with Innovative Technology, Seoul National University Hospital, Seoul 03122, Korea

[4] Department of Biomedical Engineering, Seoul National University College of Medicine, Seoul 03080, Korea

*Corresponding Author, E-mail: sungwan@snu.ac.kr

Abstract

Experiments conducted onboard the International Space Station help investigate the physiological changes that living organisms undergo in microgravity. On Earth, the two-axis clinostat serves as an alternative that can continuously change the direction of gravity and simulate microgravity conditions by time-averaging the gravity vector. However, its structural characteristics inevitably produce poles where gravity is unevenly concentrated. This study conducted a quantitative analysis and comparison of pole formation across four representative clinostat control strategies. To evaluate the poles, two quantitative indicators were defined. The commonly used control strategies, maintaining a constant angular velocity or following a random distribution, were found to induce severe poles. In contrast, when the angular velocity of the external motor followed a specifically designed reciprocal sinusoidal profile, pole formation could be significantly reduced by adjusting the ratio between the minimum and maximum angular velocities. These trends, identified through simulations, were further validated through experiments using an inertial measurement unit.

Introduction

Gravity continuously influences all living organisms on Earth. Since the 1960s, astronauts exposed to long-term microgravity environments have experienced various physiological issues, including abnormal cellular functions, immune system imbalances, and muscle atrophy [1–8]. Numerous studies have been conducted on clarifying the effects of microgravity on biological systems, including the use of the International Space Station (ISS) to provide actual microgravity environments. However, conducting experiments in the ISS is associated with high cost and scarce availability. Terrestrial methods, such as drop towers and parabolic flights, have been employed to simulate microgravity environments. However, these approaches generate microgravity only for a short duration, making them unsuitable for long-term experiments, such as cell culture or mouse experiments for observing genetic changes. Hence, researchers have focused on developing ground-based methods capable of delivering gravity-related stimuli comparable to those experienced in space.

Time-averaged simulated microgravity (taSMG) is a foundational principle behind many microgravity simulators. Although it does not provide actual microgravity at any given moment, it continuously alters the direction of gravity such that its time-averaged value converges below a certain threshold (10^{-2}–10^{-3} G) over an extended period. taSMG is physically distinct from true microgravity; nevertheless, some cell and plant experiments have shown that its biological effects resemble those observed onboard the ISS [9–15].

taSMG is achieved using a robotic hardware called a “clinostat” or “random positioning machine” [16,17], which comprises two perpendicular rotating axes (Fig. 1(a)); one actuator turns the outer frame, while the other, which is fixed on the outer frame, rotates the inner frame. This setup allows the gravity vector to point in all arbitrary directions in the spherical coordinate system defined with respect to the inner frame. Cells or animals placed in the inner stage fixed to the inner frame can be exposed to a time-averaged gravity-canceled environment.

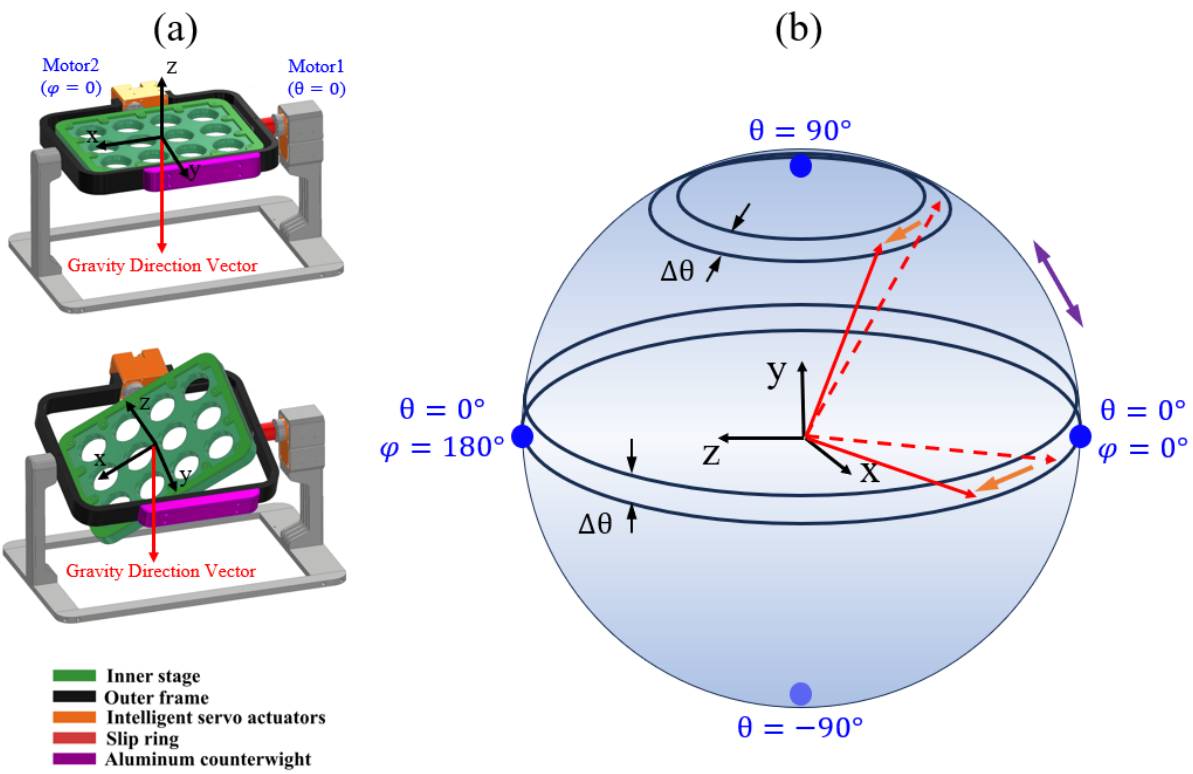

Fig. 1. Schematic of the clinostat hardware and operating principle: (a) Initial positions of Motor 1 ($\theta = 0°$) and Motor 2 ($\varphi = 0°$), and changes in the inner stage orientation with respect to variations in these angles. (b) Changes in the gravity direction vector due to orientation changes of the inner stage in the spherical coordinate system fixed to it. The latitude of the gravity direction vector is determined by the angle θ of Motor 1 (purple arrow). Once the latitude is set by angle θ, the longitude is determined by the angle φ of Motor 2 (orange arrow). Because of the smaller surface area of the latitude rings near the poles ($\theta \approx \pm 90°$) relative to those near the equator ($\theta \approx 0°$), a constant angular velocity of Motor 1 causes the gravity direction vector to concentrate more densely at high latitudes. Regions near the poles, where the gravity direction vector is more concentrated at high latitudes, are depicted with relatively darker shading.

A comprehensive review of previous clinostat development cases shows that clinostat control algorithms must enable three key functions [17–25]. First, taSMG should converge to a microgravity level

within a limited time frame. Second, the distribution of the gravity vector should be uniform. In the spherical coordinate system defined by the inner stage, the endpoint of the gravity direction vector must touch all points on the unit sphere with a uniform density as time progresses. Third, randomness should be incorporated so that the gravity vector follows a different trajectory in each trial. In most studies, the first function has been easily achieved. However, the second function, i.e., ensuring a uniform gravity vector distribution, is often not achieved or not carefully considered. Most previous control algorithms are limited to using constant angular velocities for the rotation of the two actuators in the clinostat [14,17–21,26–29]. Some studies have improved the algorithm by rotating the two axes at constant speeds while reversing the direction at randomly selected time points [17,22] or by changing the angular velocity based on a random distribution [14,30–32]. However, in such cases, due to the kinematic characteristics of the hardware, gravity tends to concentrate at opposing sides. In prior studies, the two regions with a concentrated gravity were termed “poles” [22–24,33]. As discussed in the following sections, this issue cannot be easily resolved simply by randomly adjusting the angular velocities of the actuators. Therefore, most previous studies fail to meet the second requirement. To overcome the structural limitations of the clinostat, the addition of a third actuator has also been proposed [34,35]. With this arrangement, the pole positions can be continuously altered by introducing a third axis, preventing the formation of regions where gravity is concentrated. However, the introduction of a third actuator increases the size and weight of the hardware, requiring careful consideration in the design process. Moreover, even with the use of a third axis to spread out the pole positions, they still need to be uniformly distributed across the entire spherical coordinate system. Therefore, control challenges remain.

Some studies have attempted to overcome the pole formation issue using two actuators controlled by a model-based algorithm [23,33]. TY Kim [33] applied linear and parabolic sawtooth models to prevent the generation of poles. YJ Kim et al. [23] proposed a control algorithm that can adjust the angular velocities of the outer actuator to follow a predefined mathematical model that accounts for the kinematics of the clinostat. Through this approach, they achieved not only rapid convergence to a uniformly distributed

taSMG but also to a time-averaged simulated partial gravity (taSPG). Although the results, which were validated using an inertial measurement unit (IMU), demonstrated high reliability in terms of accuracy and time efficiency, a quantitative analysis of pole reduction was not conducted.

Manzano et al. proposed a novel control algorithm [24] as an alternative method to effectively eliminate poles, where the gravity direction vector calculated using forward kinematics is directly controlled. Since the configuration space defined by the motor angles is transformed into one represented by the gravity direction vector, the pole-related issues arising from robot kinematics are precluded. Uniform taSMG is achieved by allowing the gravity vector to move randomly between evenly distributed points on a virtual sphere. The research group extended the algorithm by generating asymmetrically sized poles to realize taSPG. Instead of a sphere, they assumed a virtual ellipse and positioned one of its foci at the rotation center of the gravity vector. taSPG was achieved by allowing the gravity vector to move randomly between uniformly distributed points on the surface of the ellipse. A higher eccentricity of the ellipse results in a greater degree of taSPG. By adjusting the eccentricity, the authors successfully simulated the gravitational environments of the Moon (0.17 G) and Mars (0.38 G). Although this novel method satisfies both the second and third requirements aforementioned, it relies solely on the random movement of the gravity vector and therefore cannot guarantee the first requirement. Since the gravity direction vector undergoes a random motion on the unit sphere, a straightforward movement across the surface is unlikely, and local variations tend to dominate. Therefore, the time required to reach taSMG is expected to be relatively long and unstable, with considerable variability across different trials. Moreover, the study provides only limited quantitative experimental data.

The various control algorithms proposed for clinostat applications lack quantitative performance evaluations. To the best of our knowledge, no prior study has provided a detailed analysis of pole reduction. The presence of poles causes severe nonuniformity in the gravity vector distribution, which is a critical flaw in achieving isotropic taSMG. Most studies have either neglected this issue entirely or have only partially addressed it. Hence, it is necessary to quantitatively analyze the degree of pole formation in the application

of existing clinostat control algorithms, in order to identify more suitable algorithms and suggest guidelines for clinostat researchers. This study aimed to elucidate the strengths and weaknesses of representative control algorithms for the clinostat through software-based simulations. The representative clinostat control algorithms were chosen as four types, comprising those frequently employed in prior research together with their improved variants: (1) angular velocity following a predefined model [23]; (2) angular velocity following a sinusoidal pattern relative to the motor angle; (3) constant angular velocity [14,17–21,26–29]; and (4) angular velocity based on a uniform random distribution [14,30–32]. For each algorithm, both the degree of pole reduction and the time required to reach taSMG were computed through simulations. The control method deemed most suitable was further validated through hardware control experiments to confirm the simulation results.

Methods

Pole Reduction Analysis

A two-degree-of-freedom (2-DOF) clinostat comprises two actuators, in which Motor 1 rotates the outer frame (Fig. 1(a)) and determines the latitude of the gravity direction vector, while Motor 2 determines the longitude along the latitude defined by the angle θ of Motor 1 (Fig. 1(b)). When θ is near $\pi/2$ rad or $3\pi/2$ rad, an infinitesimal angular displacement $\Delta\theta$ covers a relatively small area, whereas near 0 rad or π rad, the same displacement $\Delta\theta$ covers a larger area. Therefore, when Motor 1 is controlled at a constant angular velocity, the gravity direction vector spends equal time in both the small and large area regions, resulting in a higher density of the gravity vector near $\theta = \pi/2$ rad or $3\pi/2$ rad, creating poles in these regions. To address this issue, Motor 1 should rotate faster near $\theta = \pi/2$ rad or $3\pi/2$ rad and slower near $\theta = 0$ rad or π rad. According to Kim et al. [23], when the angle of Motor 1 is θ, the area corresponding to a small angular displacement $\Delta\theta$ can be expressed as in Eq. (1). Thus, if Motor 1 is controlled to follow the angular velocity profile given by Eq. (2) for each θ, the poles can be completely eliminated.

$$\Delta s = 2\pi cos\theta \Delta\theta \tag{1}$$

$$w(\theta) = \frac{k}{|cos\theta|} \tag{2}$$

Here, k is an arbitrary positive constant that can be determined based on the specifications of Motor 1. However, in actual control scenarios, the angular velocity of the motor is limited, and since Eq. (2) periodically requires an infinite angular velocity, it must be constrained, as expressed in Eq. (3). w_{max} should be determined by comprehensively considering factors such as the maximum angular velocity provided by Motor 1 and any nongravitational accelerations acting on cells or animals cultured in the inner stage. In [23], the value of k was set to 0.12, and w_{max} was also set to 0.12 rad/s. Since the maximum value of $|cos\theta|$ is 1, k corresponds to the minimum value of $w(\theta)$.

$$w(\theta) = \min(\frac{k}{|cos\theta|}, w_{max}) \tag{3}$$

As an alternative to Eq. (2), a model in which the angular velocity of Motor 1 varies as a sinusoidal function of angle θ can be considered. As expressed in Eq. (4), the angular velocity reaches its maximum w_{max} at $\theta = \pi/2$ or $3\pi/2$, and its minimum w_{min} at $\theta = 0$ or π.

$$w(\theta) = (w_{max} - w_{min})(1 - |cos\theta|) + w_{min} \tag{4}$$

To evaluate the models based on Eqs. (3) and (4), simulations were conducted. The angular velocity was assumed to be updated at intervals of Δt = 0.01 s, and MATLAB® (R2024b, MathWorks Inc., Natick, MA, USA) was used as the simulation tool. When simulating the trajectory of the gravity direction vector during clinostat operation for a specified duration T h, the positions of the gravity direction vector were sampled in a quantity corresponding to N, which is calculated as follows:

$$N = \frac{3{,}600 \times T}{\Delta t} + 1 \tag{5}$$

To quantify the degree to which the gravity direction vector is concentrated at the poles, the regions within an angle θ_0 ranging from $\theta = \pi/2$ and $\theta = 3\pi/2$ are defined as poles. The density of the gravity direction vectors within these pole regions is then calculated relative to the average overall density, and this ratio is defined as the "relative pole concentration" $I(\theta_0)$. Theoretically, if $I(\theta_0)$ has a constant value of 1 for any given θ_0, it indicates that the poles are completely eliminated. In Eqs. (6) and (7), σ_0 and $\sigma_{pole}(\theta_0)$

represent the average density of the gravity direction vectors over the entire unit sphere and the density within the pole regions, respectively. $N_{pole}(\theta_0)$ is the number of times the gravity direction vector is sampled within the boundary of the two poles. We investigated the effectiveness of previously proposed control algorithms by decreasing the value of $I(\theta_0)$ toward 1.

$$\sigma_0 = \frac{N}{4\pi} \tag{6}$$

$$\sigma_{pole}(\theta_0) = \frac{N_{pole}(\theta_0)}{4\pi\times(1-cos\theta_0)} \quad (\theta_0 \leq \frac{\pi}{2}) \tag{7}$$

$$I(\theta_0) = \frac{\sigma_{pole}(\theta_0)}{\sigma_0} \tag{8}$$

To quantify the distribution of the gravity direction vectors as a function of the latitude θ, their density was calculated within the region between latitudes θ_1 and θ_2. The "gravity direction vector density" D_{θ_1,θ_2} in each region is expressed as a relative value with respect to the mean density σ_0 (Eq. (9)). In Eq. (9), N_{θ_1,θ_2} denotes the number of times the gravity direction vector is sampled within the region between latitudes θ_1 and θ_2.

$$D_{\theta_1,\theta_2} = \frac{N_{\theta_1,\theta_2}}{4\pi\times(cos\theta_1-cos\theta_2)\times\sigma_0} \tag{9}$$

For both models defined by Eqs. (3) and (4), simulations were conducted to calculate $I(\theta_0)$, with the pole angle θ_0 varied from 5° to 15° in increments of 1°. To calculate D_{θ_1,θ_2}, the variable θ_1 was increased from 0° to 80° in increments of 10°, while the interval between θ_1 and θ_2 was consistently maintained at 10°. In other words, the region from latitude 0° to 90° was divided into 10° segments, and the density of the gravity direction vectors was calculated for each segment. The variable T was set to 2.0, considering that both $I(\theta_0)$ and D_{θ_1,θ_2} become sufficiently saturated within this duration. For Eq. (3), $k = 0.1$ was set so that the minimum angular velocity would be 0.1 rad/s, and $I(\theta_0)$ and D_{θ_1,θ_2} were calculated for increasing values of w_{max}. In Eq. (4), to conduct the experiment under the same conditions as Eq. (3), w_{min} was set to 0.1 rad/s, and likewise, $I(\theta_0)$ and D_{θ_1,θ_2} were calculated for increasing values of w_{max}. Along with Eqs. (3) and (4), the same pole analysis was conducted for two classical clinostat control

methods: one in which a random value was assigned to the angular velocity of Motor 1 (Eq. (10)), and another in which Motor 1 was driven at a constant angular velocity w_c. In this study, the angular velocity profiles given by Eq. (3), Eq. (4), and Eq. (10) are referred to as "reciprocal sinusoidal profile," "sinusoidal profile," and "uniform random profile," respectively, to allow readers to understand them more intuitively.

$$w(\theta) \sim u(0.1, w_{max}) \tag{10}$$

In all the four control strategies, Motor 2 was driven at a constant angular velocity of approximately 0.1 rad/s. When the rotation periods of Motors 1 and 2 form a simple integer ratio, the gravity direction vector tends to follow repetitive, simple closed-loop trajectories. To avoid this issue, a slight deviation (within 2% of 0.1 rad/s) was allowed.

Time Required to Reach taSMG

According to previous studies, the attainment of taSMG is determined based on a threshold of 10^{-3} G, where 1G represents Earth's gravity [18,19,36]. The same standard was also adopted in this study. However, as taSMG exhibits damped oscillations rather than a monotonic decrease over time, the taSMG attainment time is defined as the last moment at which $taSMG \geq 10^3$ G holds. Previous studies did not clearly specify this criterion, which remains a notable limitation. Based on prior research, taSMG was calculated using Eqs. (11)–(13) [22–24,37]. In Eqs. (12) and (13), i denotes the index of the sampled gravity direction vectors.

$$\overrightarrow{g(\theta,\varphi)} = R_y^T(\theta)R_x^T(\varphi) = \begin{bmatrix} cos\varphi & sin\theta sin\varphi & -cos\theta sin\varphi \\ 0 & cos\theta & sin\theta \\ sin\varphi & -sin\theta cos\varphi & cos\theta cos\varphi \end{bmatrix} [0 \quad 0 \quad -1]^T$$

$$= [cos\theta sin\varphi \quad -sin\theta \quad -cos\theta cos\varphi]^T \tag{11}$$

$$g_{X,mean} = \frac{\sum_{i=1}^{N} g_{X,i}}{N},\ g_{Y,mean} = \frac{\sum_{i=1}^{N} g_{Y,i}}{N},\ g_{Z,mean} = \frac{\sum_{i=1}^{N} g_{Z,i}}{N} \tag{12}$$

$$taSMG = \sqrt{(g_{X,mean})^2 + (g_{Y,mean})^2 + (g_{Z,mean})^2} \tag{13}$$

Experimental Validation on Real Hardware

Based on the simulation results presented in the sections below, applying reciprocal sinusoidal profile was determined to be the most suitable approach to comprehensively consider both pole reduction and taSMG convergence time. Therefore, it was further validated in the experimental setup shown in Fig. 2.

The frame of the two-axis clinostat was fabricated via stereolithography 3D printing using Accura ClearVue, a polycarbonate-like material. Two intelligent servo motors (Dynamixel XD540-T270-R; ROBOTIS, Seoul, Republic of Korea), each integrated with a brushless direct current motor, an absolute encoder, and a control board, were employed to drive the two-axis rotation of the inner stage. A microcontroller (OpenRB-150; ROBOTIS, Seoul, Republic of Korea) helped control the rotational speeds of both axes based on the encoder feedback. For Motor 1, the target speed ratios ($= w_{max}/w_{min}$) of 1, 2, and 5 were realized using multiples of the minimum controllable increment, 0.229 rpm. In the case of a speed ratio of 1:1, however, the gravity direction vector tends to repeat, producing a simple closed-loop trajectory; to avoid this, a slight deviation of up to 20% (≈0.229 rpm) was allowed. Consequently, the maximum speeds of Motor 1 ($= w_{max}$) were set to 1.374, 2.290, and 5.725 rpm, respectively, while the minimum speed ($= w_{min}$) remained fixed at 1.145 rpm. As the angular velocity ratio increases, the difference between the minimum and maximum angular velocities becomes larger, requiring higher torque from the motor. Given the limited performance of the motor, control conditions demanding high torque may prevent the motor from accurately tracking the commanded angular velocity profile, resulting in control errors. To exclude unmodeled errors from the experimental results, the angular velocity ratio was limited to a maximum of 5 for clinostat operation. The speed of Motor 2 was held constant at 1.145 rpm under all the conditions to ensure consistent comparison.

To estimate the gravity direction vector in the coordinate frame of the inner stage during rotation, two methods were employed. First, the built-in absolute encoders (4096 pulse/rev) of the intelligent servos recorded the angle of each motor, and Eq. (11) was applied to compute $\overrightarrow{g(\theta,\varphi)}$ in the inner stage frame. Second, an IMU sensor (EBIMU24GV52; E2BOX, Seoul, Republic of Korea) mounted at the center of the

inner stage measured its orientation changes (Fig. 2). In this study, to minimize the influence of non-gravitational accelerations measured by the IMU, namely tangential and centrifugal accelerations, the IMU was fixed at the center of rotation. In practical experiments, as the angular velocity of the rotating sample increases, the spatial region in which taSMG remains below 10^{-3} G becomes increasingly limited, necessitating careful selection of the angular velocity based on the characteristics of the experimental subject. The Z-axis direction in the sensor frame (gravity direction vector) was transformed to the global frame by applying the quaternion conjugate provided by the IMU. To minimize long-term drift and transient noise in the IMU data, an initial offset, derived from the encoder-based angles, was applied, followed by a low-pass filter correction. Data collection was configured so that encoder readings could be transmitted every 10 ms and IMU readings every 16 ms, with all the measurements synchronized at intervals of 100 ms. A custom sketch, developed using the open-source processing environment (Processing 4.4.4; The Processing Foundation, Cambridge, MA, USA), was implemented to acquire sensor and encoder data via serial communication and save the combined data stream directly to a CSV file for subsequent analysis.

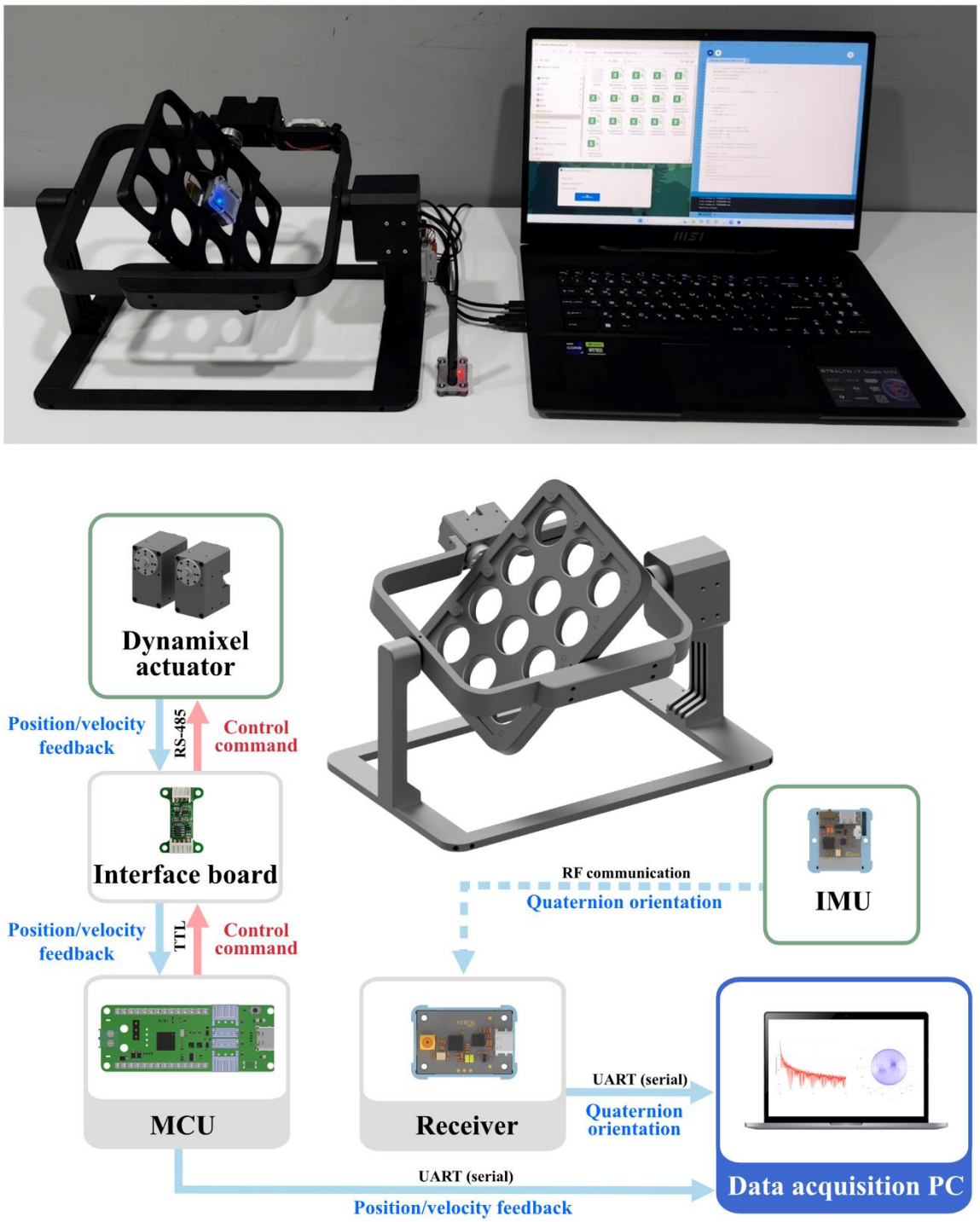

Fig. 2. Experimental setup and signal flow; the blue arrows indicate the signal flow for encoder and IMU data acquisition, red arrows indicate control commands, and the dashed line represents wireless communication.

Results

Pole Reduction Analysis

Figs. 3(a) and (b) show the pole analysis results when the angular velocity of Motor 1 follows reciprocal sinusoidal profile. As shown in Fig. 3(a), the relative pole concentration $I(\theta_0)$ tends to decrease with an increase in the pole radius θ_0. For any pole radius θ_0 between 5° and 15°, $I(\theta_0)$ gradually decreases with increasing w_{max}/w_{min} ratio. When the ratio is 1, i.e., when the angular velocity is constant, $I(5°)$ is 14.65. As the ratio increases sequentially to 2, 5, 10, 20, and 40, $I(5°)$ gradually decreases to 10.19, 4.48, 2.22, 1.33, and 1.05, respectively. A similar trend can also be observed for $I(\theta_0 \geq 6°)$. Under conditions where $w_{max}/w_{min} \geq 11.5$, $I(\theta_0 \geq 5°)$ is always less than 2, indicating that the poles are largely reduced. Fig. 3(b) shows the relative density D_{θ_1,θ_2} in each region, after dividing the latitude of the unit sphere into 10° intervals. For $w_{max}/w_{min} = 1$, severe pole formation is evident, as indicated by $D_{80,90} = 7.34$ and $D_{70,80} = 2.47$. In contrast, under the condition $w_{max}/w_{min} \geq 10$, the D_{θ_1,θ_2} value remains below 1.31, suggesting a substantial reduction in pole concentration. When $w_{max}/w_{min} \geq 5.75$, the condition $D_{80,90} \leq 2$ is always satisfied.

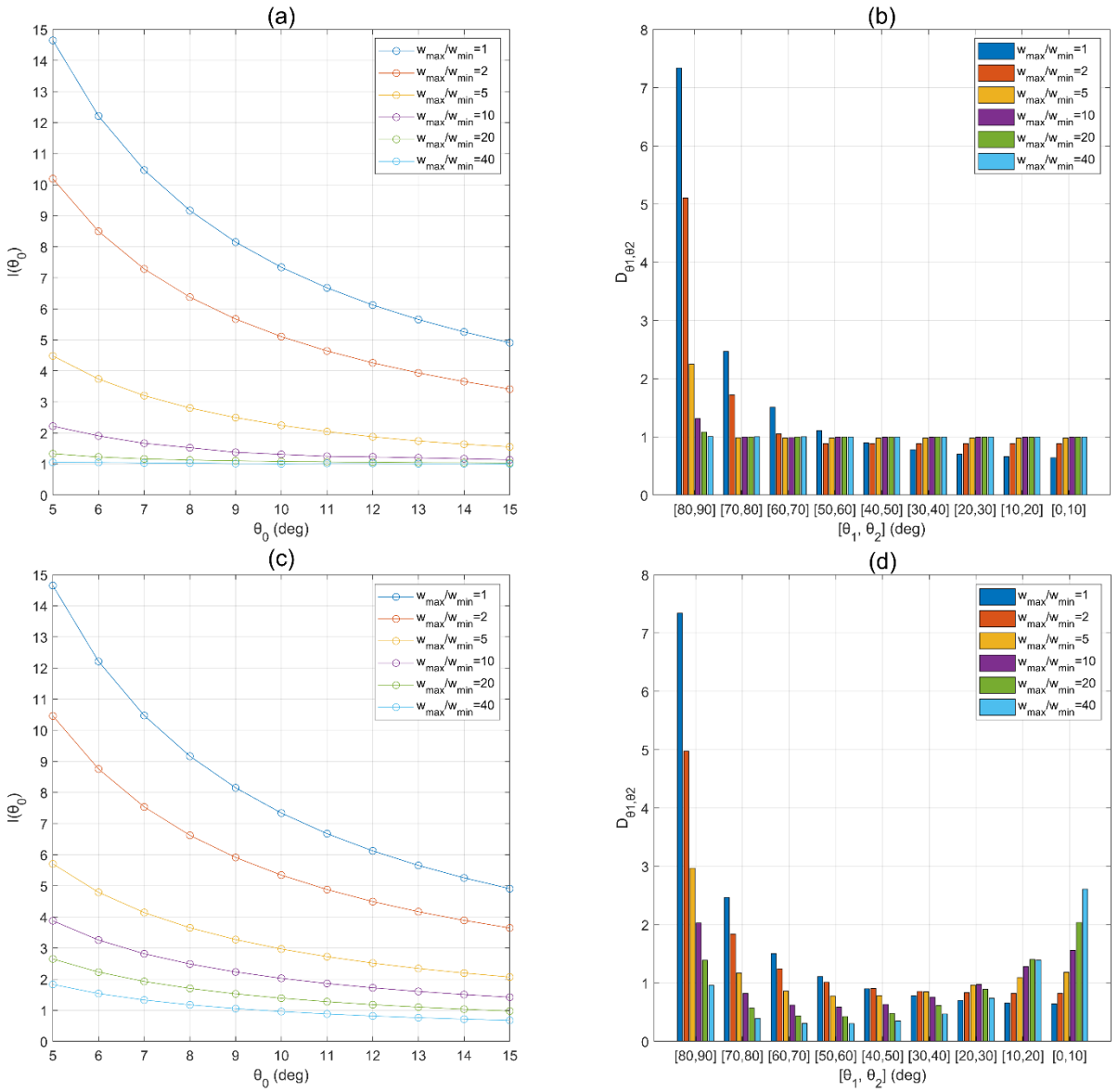

Fig. 3. Pole analysis when the angular velocity of Motor 1 follows reciprocal sinusoidal profile: (a) Relative pole concentration $I(\theta_0)$ as a function of the pole radius. (b) Gravity vector density D_{θ_1,θ_2} in each unit spherical segment. Pole analysis when the angular velocity of Motor 1 follows sinusoidal profile: (c) Relative pole concentration $I(\theta_0)$ as a function of the pole radius. (d) Gravity vector density D_{θ_1,θ_2} in each unit spherical segment.

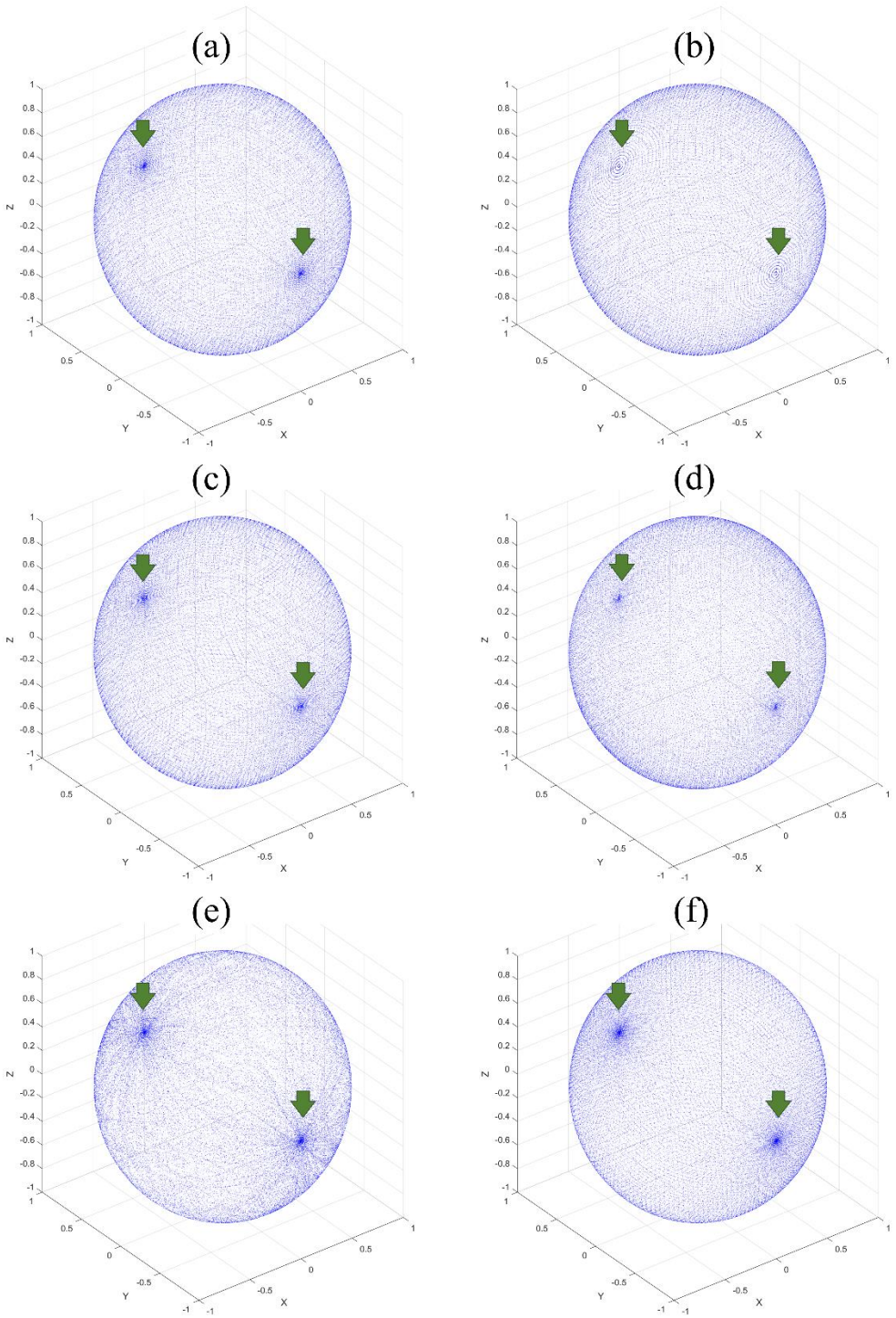

Fig. 4. Gravity direction vector distribution when the angular velocity of Motor 1 follows reciprocal sinusoidal profile: (a) $w_{max}/w_{min} = 2$, (b) $w_{max}/w_{min} = 5$. Compared with figure (a), the poles are observed to be almost eliminated in figure (b). Distribution of the gravity direction vector when the angular velocity of Motor 1 follows sinusoidal profile: (c) $w_{max}/w_{min} = 2$. (d) $w_{max}/w_{min} = 5$. Compared with figure (c), the poles are observed to be markedly reduced in figure (d). However, unlike figure (b), relatively distinct poles remain. Distribution of the gravity direction vector (e) when the angular velocity of Motor 1

follows uniform random profile and (f) when it is constant, respectively. In both the cases, figures are obtained with $w_{max}/w_{min} = 5$. However, no noticeable differences in the pole formation can be observed in either figures (e) or (f), despite variations in the w_{max}/w_{min} ratio. All the simulations for visualization assumed 2 h of clinostat operation.

Figs. 4(a) and (b) show the gravity direction vectors distributed on the unit sphere for $w_{max}/w_{min} =$ 2 and 5, respectively. Data were down-sampled every 0.1s over a duration of $T = 2$. In Fig. 4(a), gravity vectors are observed to be densely concentrated on both sides along the y-axis, whereas in Fig. 4(b), this concentration is nearly eliminated.

When the angular velocity follows sinusoidal profile, two major differences are observed compared with the case where it follows reciprocal sinusoidal profile. First, with increasing w_{max}/w_{min} ratio, the reduction in the pole concentration is relatively small. As shown in Fig. 3(c), the observed values of $I(\theta_0)$ do not sufficiently approach 1 even when the w_{max}/w_{min} ratio is 20 or 40, indicating a noticeable deviation. For example, even at a w_{max}/w_{min} ratio of 40, $I(5°)$ remains at 1.83, which is nearly twice as high as that in the case where the angular velocity follows reciprocal sinusoidal profile. As a result, sinusoidal profile is clearly less effective than reciprocal sinusoidal profile for pole reduction. The second issue is that, as the w_{max}/w_{min} ratio increases, D_{θ_1,θ_2} tends to drop below 1 near a latitude of 45°, while it increases above 1 again near a latitude of 0°. This trend becomes more pronounced as w_{max}/w_{min} increases (Fig. 3(d)). For instance, at a ratio of 40, $D_{80,90}$ reaches 0.96, suggesting effective pole elimination. However, this results in an excessive decrease in $D_{40,50}$ to 0.35 and an unnecessarily large increase in $D_{0,10}$ to 2.61. In other words, while pole formation near a latitude of 90° could be partially mitigated, the densities in the mid-latitude and low-latitude regions decreased and increased excessively, respectively.

Figs. 4(c) and (d) show the gravity direction vectors distributed on the unit sphere for $w_{max}/w_{min} =$ 2 and 5, respectively. Data were down-sampled every 0.1 s over a duration of $T = 2$. In Fig. 4(c), gravity vectors are observed to be densely concentrated on both sides along the y-axis, whereas in Fig. 4(d), this

concentration appears to be partially alleviated. In comparison with the case where the angular velocity follows reciprocal sinusoidal profile (Fig. 4(b)), two distinct poles are still evident. These findings are consistent with the observations presented in Figs. 3(a) and (c). For $w_{max}/w_{min} = 5$, the average value of $I(5° \leq \theta_0 \leq 15°)$ is 1.32 ± 0.03 times higher when the angular velocity follows sinusoidal profile, compared with that when it follows reciprocal sinusoidal profile.

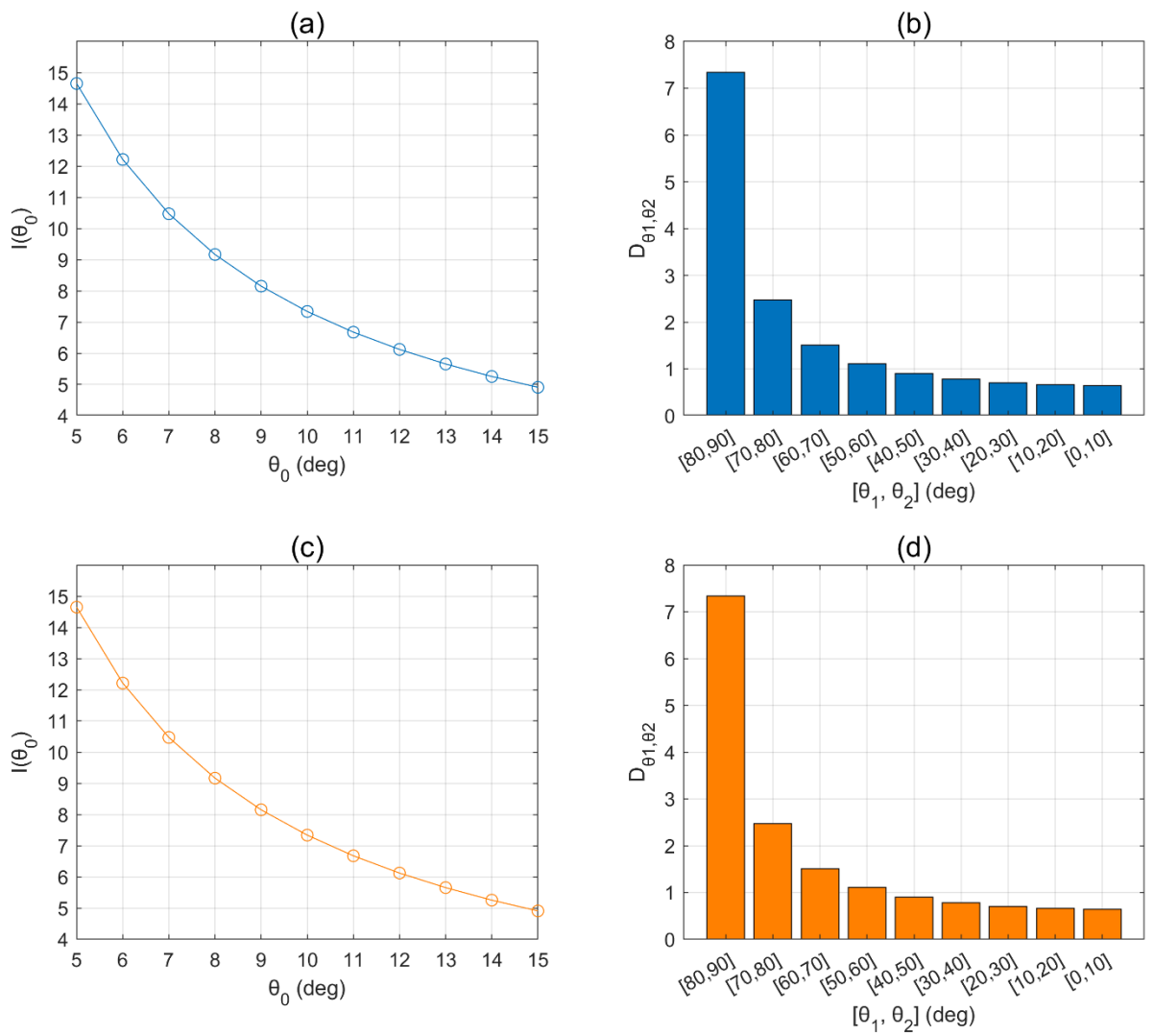

Fig. 5. Pole analysis when the angular velocity of Motor 1 follows uniform random profile: (a) Relative pole concentration $I(\theta_0)$ as a function of the pole radius. (b) Gravity vector density D_{θ_1,θ_2} in each unit spherical segment. When the angular velocity of Motor 1 is controlled based on the uniform random profile, we observe negligible difference in $I(\theta_0)$ and D_{θ_1,θ_2} with respect to w_{max}/w_{min} (CV less than 0.35% and 0.27%, respectively). Pole analysis when the angular velocity of Motor1 maintains constant value: (c) Relative pole concentration $I(\theta_0)$ as a function of pole radius. (d) Gravity vector density D_{θ_1,θ_2} in each unit spherical segment. When the angular velocity of Motor1 is controlled at a constant value w_c, we

observe negligible difference in $I(\theta_0)$ and D_{θ_1,θ_2} with respect to w_c (CV less than 0.06% and 0.05%, respectively).

When the angular velocity is determined by uniform random profile, negligible differences in the values of $I(\theta_0)$ or D_{θ_1,θ_2} were observed with respect to the w_{max}/w_{min} ratio. Regardless of the latitude range, the variations in $I(\theta_0)$ and D_{θ_1,θ_2} due to changes in the ratio w_{max}/w_{min} from 1 to 40 showed a coefficient of variance (CV) less than 0.35% and 0.27%, respectively. Even when the angular velocity was controlled at a constant value, no negligible differences in $I(\theta_0)$ or D_{θ_1,θ_2} were observed depending on the angular velocity. As in the case of uniform random profile, the errors showed a CV less than 0.06% for $I(\theta_0)$ and less than 0.05% for D_{θ_1,θ_2}. Furthermore, no statistically significant ($p > 0.05$) difference in pole formation was observed between the angular velocity controlled by the uniform random profile (Figs. 5(a) and (b)) and constant value (Figs. 5(c) and (d)). Table 1 presents the detailed results of the t-test and errors to compare pole reduction. Based on the Lilliefors test results, some data groups did not meet the normality assumption at a significance level of $p = 0.05$. Given that each independent group comprised 157 samples, Welch's t-test was subsequently applied. Both $I(\theta_0)$ and D_{θ_1,θ_2} showed an error less than 0.04% between the two angular velocity control methods (Table 1). As a result, controlling the angular velocity of the motor in a random manner did not produce a meaningful difference in pole reduction, and it resulted in the formation of poles almost the same as those observed under constant angular velocity control.

Table 1. Comparison of pole-related indices under a uniform random angular velocity and a constant angular velocity.

					$I(\theta_0)$						
Pole radius (°)	5	6	7	8	9	10	11	12	13	14	15
p-value	0.922	0.079	0.728	0.234	0.898	0.496	0.130	0.639	0.413	0.352	0.880
Error (%)	*	0.04	*	0.03	*	0.01	0.03	*	0.01	0.01	*
					D_{θ_1,θ_2}						

$[\theta_1,\theta_2]$ (°)	[0,10]	[10,20]	[20,30]	[30,40]	[40,50]	[50,60]	[60,70]	[70,80]	[80,90]
p-value	0.868	0.662	0.614	0.796	0.340	0.056	0.930	0.637	0.705
Error (%)	*	*	*	*	0.02	0.04	*	*	*

*: Errors less than 0.01%

Figs. 4(e) and (f) show the distribution of the gravity direction vectors after 2 h for the cases where the angular velocity was determined by a uniform random profile and by a constant value, respectively. The gravity direction vectors were down-sampled at intervals of 0.1 s for visualization. Although Fig. 4(e) shows a slightly more irregular distribution of the gravity direction vectors compared with Fig. 4(f), there is no notable difference in pole formation. This is consistent with the results shown in Fig. 5.

Time Required to Reach taSMG

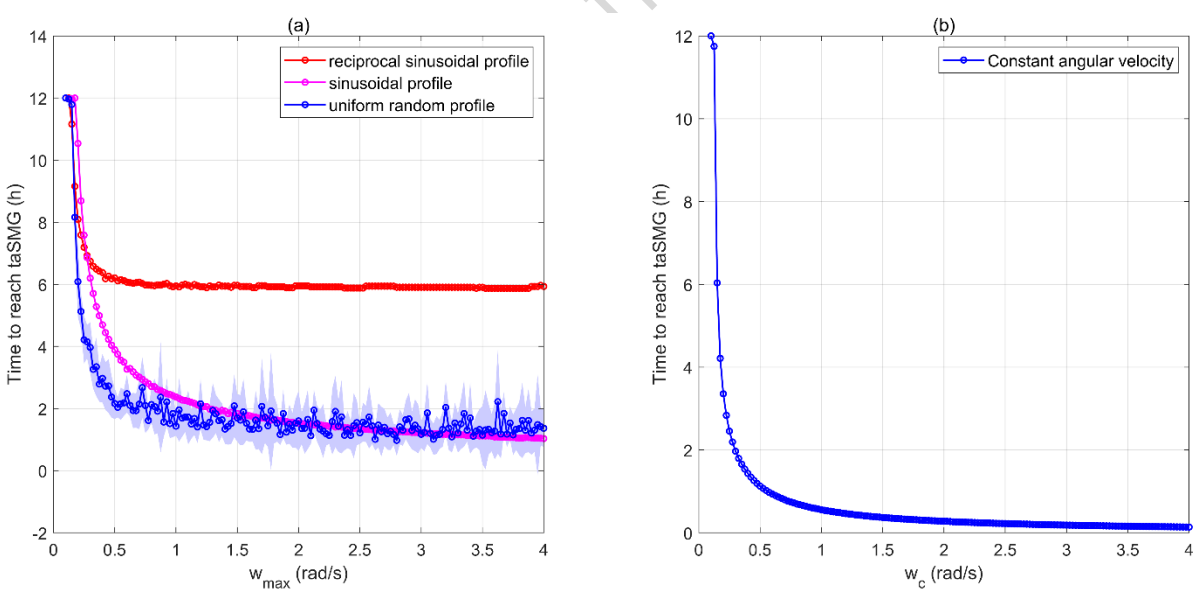

Fig. 6. (a) Time required to reach taSMG when the angular velocity of Motor 1 follows reciprocal sinusoidal, sinusoidal, or uniform random profiles. The minimum angular velocity $w_{min} = 0.1$ rad/s is fixed in all three cases, while the maximum angular velocity w_{max} is varied from 0.1 to 4.0 rad/s. The blue shading around the blue solid line represents the standard deviation when the angular velocity of Motor 1 follows uniform random profile. (b) Time required to reach taSMG when the angular velocity of Motor 1 follows a constant value w_c.

The time required to reach taSMG was calculated for each case where the angular velocities followed

reciprocal sinusoidal, sinusoidal, or uniform random profiles (Fig. 6(a)). The calculations were performed with w_{max}/w_{min} varying from 1 to 40 in increments of 0.025 (w_{min} = 0.1 rad/s). Figs. 7(a)–(c) show examples of the time-averaged gravity for $w_{max}/w_{min} = 5$. When uniform random profile was applied, variations across trials were observed, and the results were obtained by repeating the simulation 10 times. When the angular velocity was kept constant, the time required to reach taSMG was calculated as the velocity varied from 0.1 to 4.0 rad/s (Fig. 6(b)). Fig. 7(d) shows an example of the time-averaged gravity for the case with an angular velocity of 0.3 rad/s. As a representative example, we selected the case where the angular velocity of Motor 1 was 0.3 rad/s because it was equal to or close to the mean angular velocity of the other models in which w_{max} and w_{min} were 0.5 and 0.1 rad/s, respectively.

In the case of sinusoidal or uniform random profile, the time required to achieve taSMG gradually decreased with increasing w_{max}, reaching less than 2 h (Fig. 6(a)). Under a constant angular velocity control of Motor 1, the time required to achieve taSMG progressively decreased with increasing angular velocity, requiring less than 1 h to reach taSMG beyond 0.575 rad/s (Fig. 6(b)). In contrast, when applying reciprocal sinusoidal profile, we found that the time required to achieve taSMG decreased to less than 6 h once Motor 1 reached 1.1 rad/s or higher. However, a further increase in w_{max} did not reduce the taSMG time, which remained nearly constant (Fig. 6(a)).

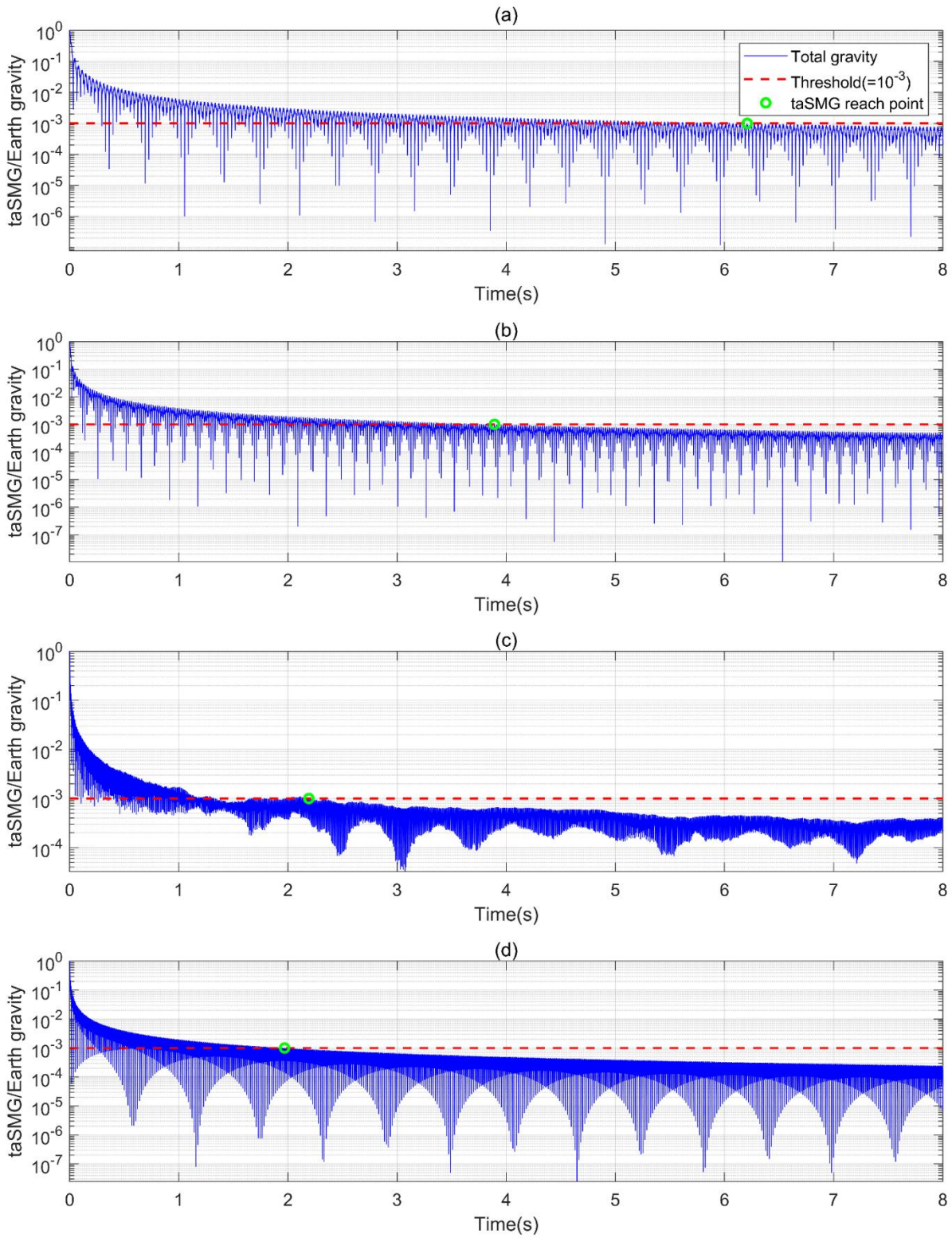

Fig. 7. Temporal change in the magnitude of the time-averaged gravity when the angular velocity of Motor 1 follows (a) reciprocal sinusoidal profile, (b) sinusoidal profile, and (c) uniform random profile, and when it is (d) a constant value. The red dashed line represents the 10^{-3} G threshold, and the green marker indicates the point at which the time-averaged gravity value permanently falls below the threshold. In (c), the shape

of the graph varies depending on the trial.

Experimental Validation on Real Hardware

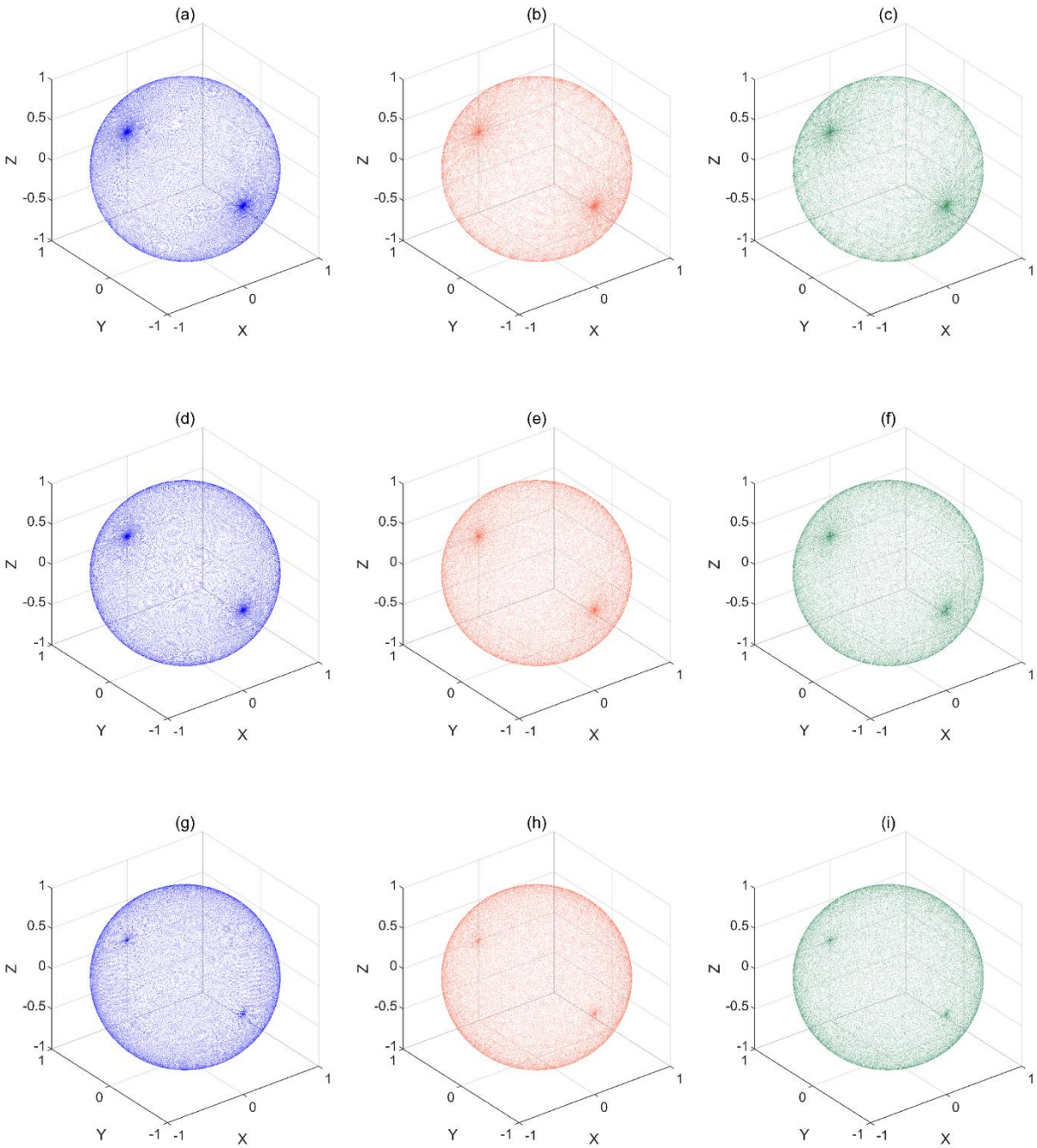

Fig. 8. Distribution of the gravity direction vectors after 12-h clinostat operation under different angular velocity ratios: (a–c) correspond to the case where the w_{max}/w_{min} ratio is 1.2, (d–f) represent the case with a ratio of 2, and (g–i) show the results for a ratio of 5. Simulation results are indicated in blue, encoder-based measurements in orange, and IMU-based measurements in green.

As shown in Fig. 8, with increasing w_{max}/w_{min} ratio, the degree of pole formation decreases, which is consistently observed in the simulation results as well as in the encoder- and IMU-based measurements. Moreover, for each angular velocity ratio, the results from the simulation, encoder-based measurements, and IMU-based measurements showed no noticeable differences.

To quantitatively analyze the degree of pole formation, numerical metrics were computed (Fig. 9). The relative pole concentration $I(\theta_0)$ showed an excellent agreement between the simulation and both encoder- and IMU-based measurements across all angular velocity ratios of 1.2, 2, and 5. In both the measurement types, the average errors were 1.56% and 1.74%, respectively (Figs. 9(a)–(c)). The average error between the encoder- and IMU-based measurements was 0.38%. Similarly, for the gravity direction vector density D_{θ_1,θ_2}, the average errors with respect to the simulation were 1.41% and 1.38% for the encoder- and IMU-based measurements (Figs. 9(d)–(f)), respectively. The average error between the encoder- and IMU-based measurements was 0.27%.

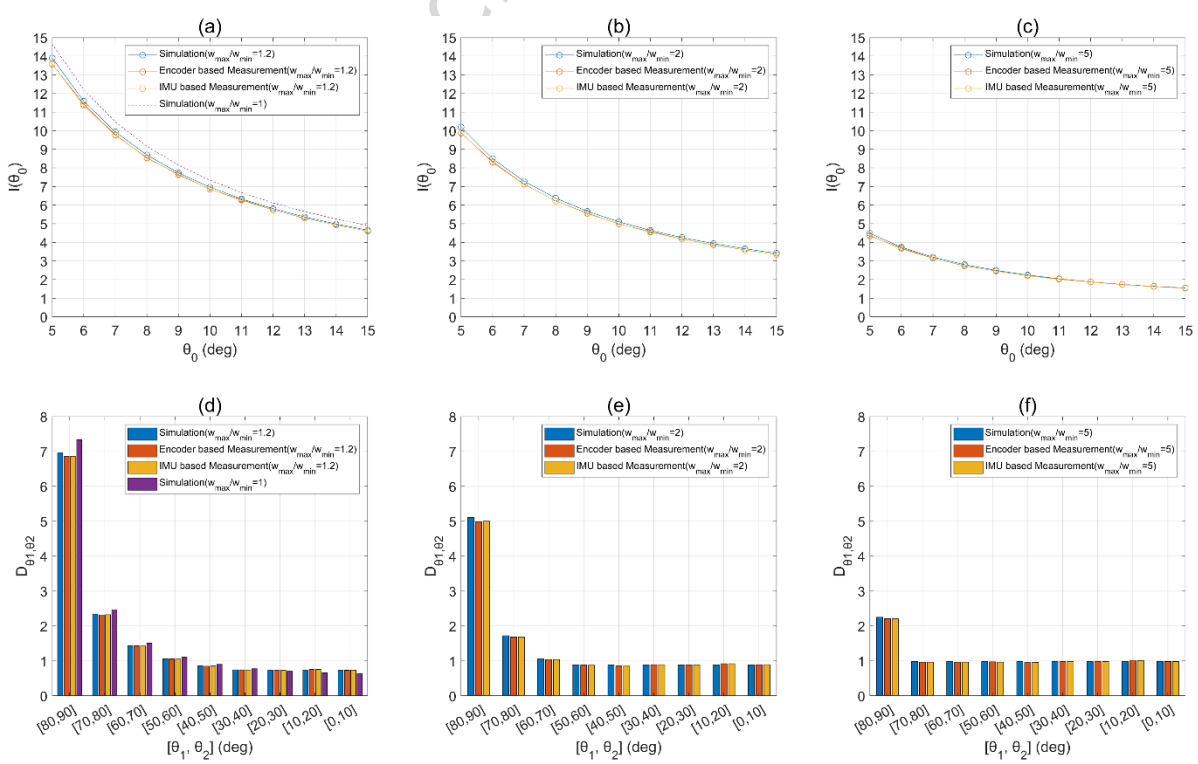

Fig. 9. Pole metrics based on clinostat experimental results: (a–c) present $I(\theta_0)$ for w_{max}/w_{min} ratios of

1.2, 2, and 5, respectively. (d–f) show D_{θ_1,θ_2} for the same respective ratios. Due to the angular velocity resolution limitations of the Dynamixel used as Motor 1, the experiment was conducted with a ratio of 1.2 instead of 1. Therefore, the simulation results for an ideal ratio of 1 are also shown in (a) and (d) for comparison.

The clinostat experimental results also confirmed the simulation results: the degree of pole formation decreased with increasing w_{max}/w_{min} ratio. Based on the IMU measurements, $I(5°)$ decreased from 13.59 to 9.89 and 4.37 as the ratio increased from 1.2 to 2 and 5, respectively (Figs. 9(a)–(c)). Similarly, $D_{80,90}$ decreased from 6.87 to 5.00 and 2.21 (Figs. 9(d)–(f)). In the local region near 90° latitude, the quantitative indices of the pole were greater in the simulation results than in the experimental results. For the simulation results, when w_{max}/w_{min} ratios were 1.2, 2, and 5, the values of $I(5°)$ were 13.90, 10.19, and 4.48, respectively, and the $D_{80,90}$ values were 6.97, 5.11, and 2.25, respectively (error vs. experimental results: approximately 1%–3%).

A slight difference was observed in the convergence behavior of the time-averaged gravity over time compared with the simulation (Fig. 10). Both the encoder- and IMU-based measurements closely matched the simulation results up to approximately 30 min, but thereafter, the experimental data deviated from the simulation and did not converge to 0 G, showing a persistent offset instead. The simulation results crossed the 10^{-2} and 10^{-3} G thresholds after 0.50 and 5.05 h, respectively. In contrast, the encoder- and IMU-based measurements crossed the 10^{-2} G threshold after 0.58 and 0.80 h, respectively, but did not reach the 10^{-3} G threshold thereafter. The actual clinostat operation results reached a saturation point corresponding to an offset after approximately 2 h. The encoder- and IMU-based measurements maintained offset levels of approximately 2.7×10^{-3} and 5.8×10^{-3} G, respectively.

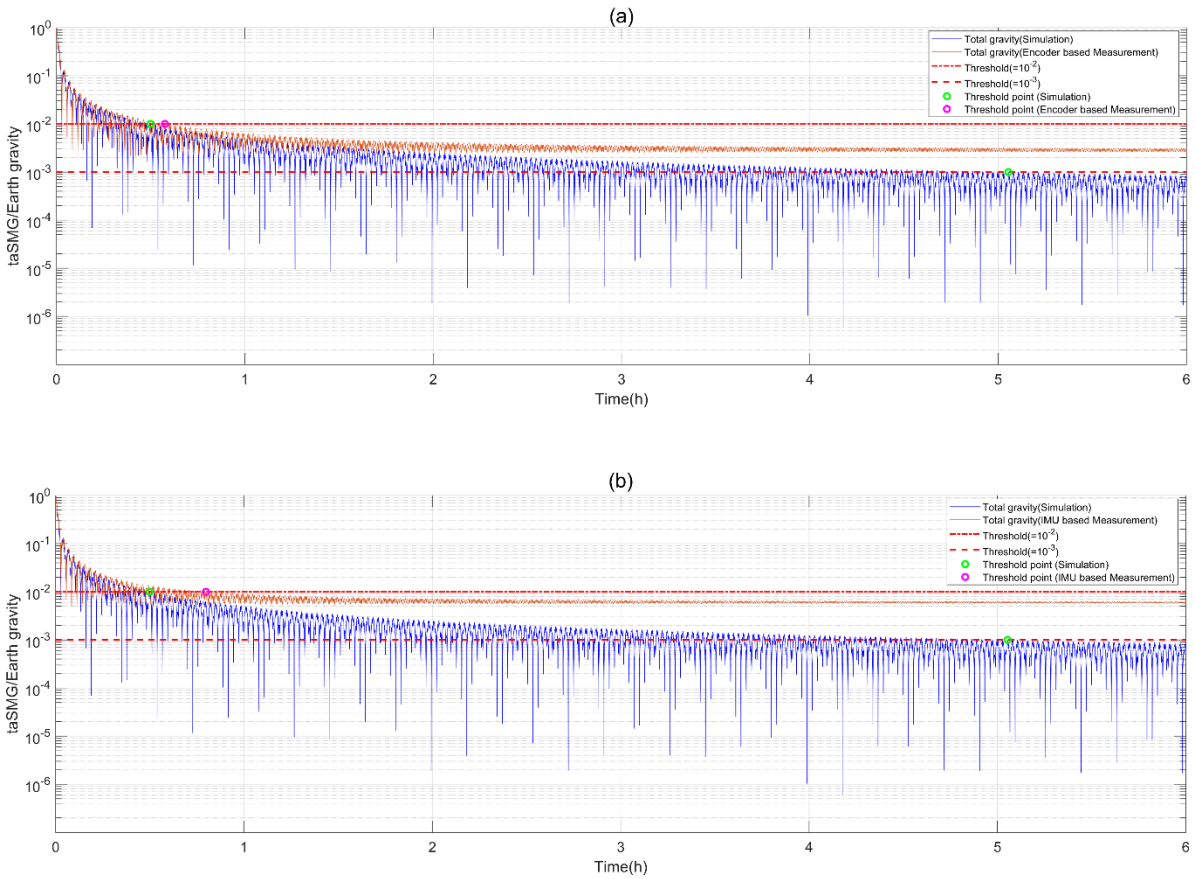

Fig. 10. Temporal changes in the time-averaged gravity vector. The dash-dot and dashed lines indicate the 10^{-2} and 10^{-3} G thresholds, respectively. In (a), the brown curve shows the time-averaged gravity measured using the encoder of Motor 1, while in (b), the brown curve shows the result based on IMU measurements. In both (a) and (b), the blue graphs represent the simulation results used for comparison. Points where the experimental and simulation results cross the thresholds are marked with pink and green circular markers, respectively.

Discussion

This study investigated how the gravity vector distribution acting on the internal stage of a clinostat is affected by different angular velocity control strategies applied to the motor that rotates the outer frame. An ideal clinostat algorithm should provide a uniform distribution of the gravity direction vector [23,24], and therefore, regions of concentrated gravity known as poles should not appear. Both reciprocal sinusoidal and sinusoidal profiles, which are aimed at reducing the duration for which the gravity direction vector remains in pole-forming regions, effectively contributed to pole reduction. However, a comparison between Figs. 3(a) and (c) showed that reciprocal sinusoidal profile is more effective in reducing these poles and that in

the case of sinusoidal profile, increasing the w_{max}/w_{min} ratio to suppress the poles resulted in undesirable distortions in the gravity direction vector density, with an excessive decrease in the mid-latitude regions and an excessive increase in the low-latitude regions (Fig. 3(d)). The application of reciprocal sinusoidal profile accurately compensates for the latitude-dependent variation in the area on the spherical coordinate system formed by the infinitesimal change in the rotation angle of Motor 1 (Fig. 1(b)). The only remaining limitation that prevents complete elimination of the poles is the angular velocity constraint w_{max}. sinusoidal profile only approximates Eq. (2) without any analytical justification, resulting in distortions due to the differences between the two equations.

However, when the angular velocity follows reciprocal sinusoidal profile, the time required to reach taSMG is significantly longer compared with that when it follows sinusoidal profile (Fig. 6(a)). In the latter case, the time to reach taSMG gradually decreased with increasing w_{max}/w_{min}, whereas in the former case, it no longer decreased beyond approximately 5.9 h. This is because, in the case of sinusoidal profile, the angular displacement, expressed as an integral of $w(\theta)$ with respect to θ, increased linearly with increasing w_{max}/w_{min}, which in turn continuously reduced the time required to traverse the same angular displacement. In contrast, in the case of reciprocal sinusoidal profile, even if w_{max} increased, the resulting increase in the angular displacement remained relatively limited. As a result, applying sinusoidal profile was relatively more advantageous in terms of the time required to reach taSMG.

In terms of pole formation and the time required to reach taSMG, reciprocal sinusoidal profile and sinusoidal profile each have their respective advantages and disadvantages. However, considering previous taSMG-based experimental designs on cell cultivation (≥1 day) [18,19,36,37] or rat observation (≥12 h) [30,31], the inability to shorten the time to reach taSMG below approximately 6 h is not considered a critical issue. In principle, clinostat-based studies are conducted over relatively long durations, compared with parabolic flight or drop tower experiments. Unlike the taSMG arrival time issue, pole formation results in a nonuniform gravity vector distribution on the specimen inside the inner stage, which cannot be overlooked. From the perspective of the specimen, it experiences gravity concentrated in the directions where the two

poles are located, and the pole issue cannot be concluded as resolved, simply because the gravitational forces in these two directions are canceled out by their physical vector summation. In conclusion, applying reciprocal sinusoidal profile is more appropriate than applying sinusoidal profile in clinostat-based experiments.

Even when the angular velocity of Motor 1 was determined based on uniform random profile, the pole issue remained entirely unresolved. A statistical analysis confirmed that the extent of pole formation was identical to that observed when the angular velocity was maintained constant (Table 1). It is possible to mistakenly assume that controlling the angular velocity based on a random distribution would resolve the pole issue. While the use of randomly selected angular velocities helps prevent the formation of repeating closed-loop trajectories of the gravity vector [17,22,30,31], a quantitative analysis revealed that the degree of pole formation was still identical to that observed under a constant angular velocity. According to latest reports, it is necessary to either control the angular velocity of the motor rotating the outer frame based on reciprocal sinusoidal profile [23], or apply forward kinematics to transform the configuration space [24]. When the angular velocity is determined by a uniform random distribution, varying the range of the distribution has no effect on pole formation (CV less than 0.35% and 0.27%, respectively for $I(\theta_0)$ and D_{θ_1,θ_2}). Even when the angular velocity is kept constant, the extent of pole formation does not depend on its value (CV less than 0.06% and 0.05%, respectively for $I(\theta_0)$ and D_{θ_1,θ_2}). In conclusion, with regard to pole elimination, the control based on reciprocal sinusoidal profile has a clear comparative advantage over the other control methods investigated in this study.

When the angular velocity was controlled according to uniform random profile, randomness was involved, resulting in variations in the taSMG arrival time across trials. With an increase in the w_{max}/w_{min} ratio, the mean taSMG arrival time consistently decreased, and for conditions with a ratio of 2 or higher, values similar to those obtained by applying sinusoidal profile were obtained (Fig. 6(a)). This is because, in both sinusoidal profile and uniform random profile, the average angular velocity of Motor 1, or its expected value, is $(w_{max} + w_{min})/2$, and therefore, the predicted position of the gravity direction vector

after a certain elapsed time is the same. Applying uniform random profile is advantageous for ensuring the validity of the cell or animal experimental results because it ensures the non-repetitiveness of the trajectory. However, the issue of the robustness of the taSMG arrival time should also be considered. If the exposure time of cells or animals to the time-averaged gravity is not sufficiently long, taSMG may not be achieved in certain trials.

When the angular velocity of Motor 1 was controlled at a constant rate, the taSMG arrival time was the shortest. Even when comparing the conditions in which the average angular velocity of Motor 1, calculated as $(w_{max} + w_{min})/2$ for reciprocal sinusoidal and sinusoidal profiles, matched the constant angular velocity w_c, the constant angular velocity control still resulted in faster taSMG arrival (Figs. 6(a) and (b)). When applying sinusoidal profile, the taSMG arrival times were 3.89 h and 2.37 h for w_{max} values of 0.5 and 1 rad/s, respectively, with $w_{min} = 0.1$ rad/s. In contrast, when the angular velocity was controlled at constant values of $w_c = 0.3$ rad/s and 0.55 rad/s, the arrival times were 1.97 and 1.02 h, respectively, which were shorter, despite the same average angular velocity being applied. This is believed to be because, in the absence of velocity changes, the symmetry of the gravity direction vector is established more quickly, allowing faster taSMG arrival. As a result, controlling the angular velocity at a constant rate is the least favorable for pole formation, along with applying uniform random profile, but it is the most advantageous in terms of the taSMG arrival time. Therefore, the most widely used control strategy, which maintains a constant angular velocity, may require experimental validation to confirm that variations in the uniformity and non-repetitiveness of gravity vector changes experienced by the subjects do not alter physiological responses.

The actual clinostat hardware control results were validated to confirm whether the trends observed in the simulation were consistent with the measurement results. The experimental results were doubly validated using two methods, one estimating the gravity vector from the encoder angle data of the motor and the other directly measuring the gravity vector using an IMU. Both the relative pole concentration $I(\theta_0)$ and the gravity direction vector density D_{θ_1,θ_2}, which are quantitative indicators for assessing the

degree of pole formation, showed that the encoder and IMU measurement results closely matched the simulation results (error < 1.8%), with a negligible error between the two measurement methods themselves (error < 0.4%). This not only confirms that the trends derived from the simulation results are accurately maintained in the actual hardware control but also suggests that in future experiments, the simulation and encoder-based measurement methods can sufficiently replace the IMU measurement results.

There is a slight discrepancy between the simulation results and the experimental measurements in terms of the convergence trend of the time-averaged gravity over time. In the simulation, the time-averaged gravity calculated using Eqs. (11)–(13) continuously decreased, reaching below the 10^{-3} G threshold. However, in the actual experiments, both the encoder- and IMU-based measurements exhibited offsets of approximately 2.7×10^{-3} and 5.8×10^{-3} G, respectively, and did not show further decreasing trends. Both the measurements showed a tendency for the time-averaged gravity values on the y-axis not to converge, indicating that this was not simply an instrumentation error. There was a slight distortion causing Motor 1 to rotate the outer frame marginally faster in a specific direction. Although this distortion is a minor error, which is difficult to detect in a single rotation, it accumulates over the 12-h clinostat operation and manifests as a significant error in this experiment, which requires a very precise level of convergence (10^{-3} G). As shown in Fig. 1(a), Motor 2, which drives the rotation of the inner frame, is mounted at one end of the outer frame, resulting in an offset of the outer frame's center of mass toward the Motor 2 side rather than along the rotation axis. To minimize the stall torque imposed on Motor 1 by bringing the center of mass of the clinostat hardware closer to the rotation axis, a counterweight was installed. However, complete compensation was not achieved. After detaching Motor 1 mounted on the outer frame, the stall torque was remeasured, and a value of 0.063 Nm (=0.5N×0.126m) was obtained. Consequently, the torque required from Motor 1 differs depending on whether Motor 2 is moving downward or upward. Although the controller embedded in the Dynamixel minimizes such errors, they remain significant for achieving the highly precise condition of 10^{-3} G. A technical approach can be considered to eliminate this error. First, the taSPG algorithm [23], which creates an imbalance in the formation degree of the poles on both sides, can

be applied to tune the system so that the pole opposite to the direction of greater gravity vector accumulation becomes slightly more dominant. The second approach is to design a three-axis clinostat. In this study, slight error accumulation occurred in both Motors 1 and 2 due to factors, such as actuator manufacturing precision; however, the distortion from Motor 2 did not manifest as an issue in the experimental results. On examining the third column of the rotation transformation matrix in Eq. (11), we find that the first and third rows, which determine the x and z components of the gravity direction vector, include the angles of both Motors 1 and 2 multiplied together. This causes any minor distortion in one motor to be dispersed by the other motor. However, the *y* component includes only the angle of Motor 1; therefore, the small error in the angle directly led to distortion in the experimental results. Such offsets can be mitigated by adding the one more axis such that each component is related to the angular displacements of two or more motors.

Data availability

These data that support the findings of this study are available from the corresponding author upon reasonable request.

References

[1] R.H. Fitts, S.W. Trappe, D.L. Costill, P.M. Gallagher, A.C. Creer, P.A. Colloton, J.R. Peters, J.G. Romatowski, J.L. Bain, D.A. Riley, Prolonged space flight-induced alterations in the structure and function of human skeletal muscle fibres, J. Physiol. 588 (2010) 3567–3592. https://doi.org/10.1113/jphysiol.2010.188508.

[2] D.A. Riley, J.L. Bain, J.L. Thompson, R.H. Fitts, J.J. Widrick, S.W. Trappe, T.A. Trappe, D.L. Costill, Decreased thin filament density and length in human atrophic soleus muscle fibers after spaceflight, J. Appl. Physiol. (1985). 88 (2000) 567–572. https://doi.org/10.1152/jappl.2000.88.2.567.

[3] S.W. Trappe, T.A. Trappe, G.A. Lee, J.J. Widrick, D.L. Costill, R.H. Fitts, Comparison of a space shuttle flight (STS-78) and bed rest on human muscle function, J. Appl. Physiol. (1985). 91 (2001) 57–64.

https://doi.org/10.1152/jappl.2001.91.1.57.

[4] K.M. Baldwin, R.E. Herrick, E. Ilyina-Kakueva, V.S. Oganov, Effects of zero gravity on myofibril content and isomyosin distribution in rodent skeletal muscle, FASEB J. 4 (1990) 79–83. https://doi.org/10.1096/fasebj.4.1.2136840.

[5] M.L. Lewis, J.L. Reynolds, L.A. Cubano, J.P. Hatton, B.D. Lawless, E.H. Piepmeier, Spaceflight alters microtubules and increases apoptosis in human lymphocytes (Jurkat), FASEB J. 12 (1998) 1007–1018. https://doi.org/10.1096/fasebj.12.11.1007.

[6] D. Williams, A. Kuipers, C. Mukai, R. Thirsk, Acclimation during space flight: Effects on human physiology, CMAJ. 180 (2009) 1317–1323. https://doi.org/10.1503/cmaj.090628.

[7] S.K. Mehta, R.P. Stowe, A.H. Feiveson, S.K. Tyring, D.L. Pierson, Reactivation and shedding of cytomegalovirus in astronauts during spaceflight, J. Infect. Dis. 182 (2000) 1761–1764. https://doi.org/10.1086/317624.

[8] J.B. Boonyaratanakornkit, A. Cogoli, C.F. Li, T. Schopper, P. Pippia, G. Galleri, M.A. Meloni, M. Hughes-Fulford, Key gravity-sensitive signalling pathways drive T cell activation, FASEB J. 19 (2005) 2020–2022. https://doi.org/10.1096/fj.05-3778fje.

[9] A. Villa, S. Versari, J.A. Maier, S. Bradamante, Cell behavior in simulated microgravity: A comparison of results obtained with RWV and RPM, Gravit. Space Biol. Bull. 18 (2005) 89–90.

[10] J.P. Hatton, F. Gaubert, M.L. Lewis, Y. Darsel, P. Ohlmann, J.P. Cazenave, D. Schmitt, The kinetics of translocation and cellular quantity of protein kinase C in human leukocytes are modified during spaceflight, FASEB J. 13(Suppl) (1999) S23–S33. https://doi.org/10.1096/fasebj.13.9001.s23.

[11] M. Cogoli-Greuter, The lymphocyte story—An overview of selected highlights on the in vitro activation of human lymphocytes in space, Microgravity Sci. Technol. 25 (2014) 343–352. https://doi.org/10.1007/s12217-014-9362-4.

[12] M. Schwarzenberg, P. Pippia, M.A. Meloni, G. Cossu, M. Cogoli-Greuter, A. Cogoli, Signal transduction in T lymphocytes-A comparison of the data from space, the free fall machine and the

random positioning machine, Adv. Space Res. 24 (1999) 793–800. https://doi.org/10.1016/S0273-1177(99)00075-7.

[13] I. Walther, P. Pippia, M.A. Meloni, F. Turrini, F. Mannu, A. Cogoli, Simulated microgravity inhibits the genetic expression of interleukin-2 and its receptor in mitogen-activated T lymphocytes, FEBS Lett. 436 (1998) 115–118. https://doi.org/10.1016/S0014-5793(98)01107-7.

[14] T. Hoson, S. Kamisaka, Y. Masuda, M. Yamashita, B. Buchen, Evaluation of the three-dimensional clinostat as a simulator of weightlessness, Planta. 203(Suppl) (1997) S187–S197. https://doi.org/10.1007/PL00008108.

[15] M. Nishikawa, H. Ohgushi, N. Tamai, K. Osuga, M. Uemura, H. Yoshikawa, A. Myoui, The effect of simulated microgravity by three-dimensional clinostat on bone tissue engineering, Cell Transplant. 14 (2005) 829–835. https://doi.org/10.3727/000000005783982477.

[16] J.J.W.A. van Loon, Some history and use of the random positioning machine, RPM, in gravity related research, Adv. Space Res. 39 (2007) 1161–1165. https://doi.org/10.1016/j.asr.2007.02.016.

[17] A.G. Borst, J.J.W.A. van Loon, Technology and developments for the random positioning machine, RPM, Microgravity Sci. Technol. 21 (2009) 287–292. https://doi.org/10.1007/s12217-008-9043-2.

[18] Y.J. Kim, A.J. Jeong, M.J. Kim, C.W. Lee, S.-K. Ye, S. Kim, Time-averaged simulated microgravity (taSMG) inhibits proliferation of lymphoma cells, L-540 and HDLM-2, using a 3D clinostat, Biomed. Eng. OnLine. 16 (2017) 48. https://doi.org/10.1186/s12938-017-0337-8.

[19] A.J. Jeong, Y.J. Kim, M.H. Lim, H. Lee, K. Noh, B.-H. Kim, J.W. Chung, C.-H. Cho, S. Kim, S.-K. Ye, Microgravity induces autophagy via mitochondrial dysfunction in human Hodgkin's lymphoma cells, Sci. Rep. 8 (2018) 14646. https://doi.org/10.1038/s41598-018-32965-3.

[20] S.M. Kim, H. Kim, D. Yang, J. Park, R. Park, S. Namkoong, J.I. Lee, I. Choi, H.-S. Kim, H. Kim, J. Park, An experimental and theoretical approach to optimize a three-dimensional clinostat for life science experiments, Microgravity Sci. Technol. 29 (2017) 97–106. https://doi.org/10.1007/s12217-016-9529-2.

[21] D. Kim, Q.T.T. Nguyen, S. Lee, K.-M. Choi, E.-J. Lee, J.Y. Park, Customized small-sized clinostat using 3D printing and gas-permeable polydimethylsiloxane culture dish, npj Microgravity. 9 (2023) 63. https://doi.org/10.1038/s41526-023-00311-1.

[22] S.L. Wuest, S. Richard, I. Walther, R. Furrer, R. Anderegg, J. Sekler, M. Egli, A novel microgravity simulator applicable for three-dimensional cell culturing, Microgravity Sci. Technol. 26 (2014) 77–88. https://doi.org/10.1007/s12217-014-9364-2.

[23] Y.J. Kim, M.H. Lim, B. Jeon, D.H. Choi, H. Lee, A.J. Jeong, M.J. Kim, J.W. Park, J.L. Ku, S.Y. Jeong, S.K. Ye, Y. Kim, S. Kim, Manufacturing and control of a robotic device for time-averaged simulated micro and partial gravity of a cell culture environment, Int. J. Control Autom. Syst. 18 (2020) 53–64. https://doi.org/10.1007/s12555-019-0238-7.

[24] A. Manzano, R. Herranz, L.A. Den Toom, S. te Slaa, G. Borst, M. Visser, F.J. Medina, J.J.W.A. van Loon, Novel, Moon and Mars, partial gravity simulation paradigms and their effects on the balance between cell growth and cell proliferation during early plant development, npj Microgravity. 4 (2018) 9. https://doi.org/10.1038/s41526-018-0041-4.

[25] T.G. Hammond, J.M. Hammond, Optimized suspension culture: The rotating-wall vessel, Am. J. Physiol. Ren. Physiol. 281 (2001) F12–F25. https://doi.org/10.1152/ajprenal.2001.281.1.F12.

[26] J.L. Clary, C.S. France, K. Lind, R. Shi, J.S. Alexander, J.T. Richards, R.S. Scott, J. Wang, X.H. Lu, L. Harrison, Development of an inexpensive 3D clinostat and comparison with other microgravity simulators using *Mycobacterium marinum*, Front. Space Technol. 3 (2022) 1032610. https://doi.org/10.3389/frspt.2022.1032610.

[27] S.C. Kim, M.J. Kim, J.W. Park, Y.K. Shin, S.Y. Jeong, S. Kim, J.L. Ku, Effects of simulated microgravity on colorectal cancer organoids growth and drug response, Sci. Rep. 14 (2024) 25526. https://doi.org/10.1038/s41598-024-76737-8.

[28] D.H. Choi, B. Jeon, M.H. Lim, D.H. Lee, S.K. Ye, S.Y. Jeong, S. Kim, 3D cell culture using a clinostat reproduces microgravity-induced skin changes, npj Microgravity. 7 (2021) 20.

https://doi.org/10.1038/s41526-021-00148-6.

[29] M. Malczyk, T. Blachowicz, A. Ehrmann, Coupled system of dual-axis clinostat and Helmholtz cage for simulated microgravity experiments, Appl. Sci. 14 (2024) 9517. https://doi.org/10.3390/app14209517.

[30] C. Song, T. Kang, K. Gao, X. Shi, M. Zhang, L. Zhao, L. Zhou, J. Guo, Preparation for mice spaceflight: Indications for training C57BL/6J mice to adapt to microgravity effect with three-dimensional clinostat on the ground, Heliyon. 9 (2023) e19355. https://doi.org/10.1016/j.heliyon.2023.e19355.

[31] V.V. Yotov, J. Marovska, V. Turiyski, S.I. Ivanov, A new random positioning machine modification applied for microgravity simulation in laboratory experiments with rats, Inventions. 7 (2022) 85. https://doi.org/10.3390/inventions7030085.

[32] Y. Ye, W. Xie, Z. Ma, X. Wang, Y. Wen, X. Li, H. Qi, H. Wu, J. An, Y. Jiang, X. Lu, G. Chen, S. Hu, E.A. Blaber, X. Chen, L. Chang, W. Zhang, Conserved mechanisms of self-renewal and pluripotency in mouse and human ESCs regulated by simulated microgravity using a 3D clinostat, Cell Death Discov. 10 (2024) 68. https://doi.org/10.1038/s41420-024-01846-2.

[33] T.Y. Kim, Theoretical study on microgravity and hypogravity simulated by random positioning machine, Acta Astronaut. 177 (2020) 684–696. https://doi.org/10.1016/j.actaastro.2020.07.047.

[34] A. Rojas-Moreno, F. Santos-Rodriguez, Design of a novel 3DOF clinostat to produce microgravity for bioengineering applications, in: Proc IEEE XXV Int Conf Electron Electr. Eng. Comput. (INTERCON), August 2018, IEEE, New York, 2018, pp. 1–4. https://doi.org/10.1109/INTERCON.2018.8526401.

[35] Cacayurin CRC, De Chavez JCL, Lansangan MCG, Lucas CB, Villanueva JJD, Concepcion R II, Relano RJ, Bandala A (2023) An engineered design of 3-axis clinostat for simulated gravity experiments in astrobotany. In: Proc IEEE 15th Int Conf Humanoid Nanotechnol Inf Technol Commun Control Environ Manag (HNICEM), November 2023.

[36] J. Braveboy-Wagner, P.I. Lelkes, Impairment of 7F2 osteoblast function by simulated partial gravity

in a Random Positioning Machine, npj Microgravity. 8 (2022) 20. https://doi.org/10.1038/s41526-022-00202-x.

[37] T. Benavides Damm, I. Walther, S.L. Wüest, J. Sekler, M. Egli, Cell cultivation under different gravitational loads using a novel random positioning incubator, Biotechnol. Bioeng. 111 (2014) 1180–1190. https://doi.org/10.1002/bit.25179.

Acknowledgment

This work was supported by the National Research Foundation of Korea (NRF) grant funded by the Korea government (MSIT) (No. RS-2024-00458826).

It was also supported by Industrial Technology Innovation R&D Program of MOTIE/KEIT (Project No. 25421092), Development of a therapeutic endoscopic system incorporating a motorized autonomously controlled endoscopic scope - featuring over 5,000 cycles of durability, bending capability exceeding 180°, and IPX7 waterproof rating - and an AI-based image processing unit, aimed at localization of endoscopy systems and improving the success rate of endoscopic treatments.

Author contributions

Y.J.K. proposed the indices for pole evaluation, conducted simulations, and drafted the manuscript. S.P. fabricated clinostat hardware, performed IMU-based experiments, and drafted the manuscript. Y.J.K. and S.P. contributed equally to this work. As the corresponding author, S.K. supervised the entire research process and the preparation of the manuscript.

Competing interests

The authors declare no competing interests.